# Performance and status of beamline BL8 at SLRI for X-ray absorption spectroscopy

**Wantana Klysubun,\* Panidtha Sombunchoo, Weeraya Deenan and Chanapa Kongmark**

Synchrotron Light Research Institute, 111 University Avenue, Muang, Nakhon Ratchasima 30000, Thailand. E-mail: wantana@slri.or.th

Beamline BL8 of the Synchrotron Light Research Institute (Thailand) is routinely operated for X-ray absorption spectroscopy (XAS) in an intermediate photon energy range (1.25–10 keV). The photon energy is scanned by using a double-crystal monochromator, the crystal pair of which can be interchanged among KTP(011), InSb(111), Si(111) and Ge(220). The experimental set-up conveniently facilitates XAS measurements in transmission and fluorescence-yield modes at several *K*-edges of elements ranging from magnesium to zinc. Instrumentation and specification of the beamline and the XAS station are described, together with the determination of the available photon flux [0.1–6 $\times$ $10^{10}$ photon s$^{-1}$ (100 mA)$^{-1}$], energy resolution (1–5 $\times$ $10^{-4}$) and stability of photon energy calibration (0.07 eV), representing the beamline performance. Data quality and accuracy of XANES and EXAFS measured at BL8 are compared with those of other well established beamlines. A noted distinction of BL8 is its relatively high sensitivity for studying phosphorous, sulfur and chlorine in diluted systems and its maximum beam size of 14 mm (width) $\times$ 1 mm (height), which is suitable for bulk characterization.

## 1. Introduction

X-ray absorption spectroscopy (XAS) has been widely utilized for determining the chemical speciation, oxidation state and local atomic structure of an absorbing element of interest in many research areas, for example material science (Radi-savljevic *et al.*, 2010; Limpijumnong *et al.*, 2011; Baldini *et al.*, 2011), biochemistry (Freedman *et al.*, 1988; Day *et al.*, 2011; Neidig *et al.*, 2011), environmental science (O'Day *et al.*, 1998; Suksabye *et al.*, 2007; Prietzel *et al.*, 2011) and archaeology (Arletti *et al.*, 2008; Cotte *et al.*, 2010; Klysubun *et al.*, 2011). The versatility of XAS lies in (i) its capability to probe any element selectively at its absorption onset by taking advantage of the tunability of synchrotron radiation, (ii) the short-range atomic interaction within a few coordination shells, imposing no restriction on applicable sample phase and crystallinity, and (iii) follow-up atomic relaxation processes of photoelectron and X-ray fluorescence emissions allowing alternative electron-yield (EY) and fluorescence-yield (FY) set-ups to collect XAS signals, other than transmission (TM) measurements. In the latter case, the evolution of FY solid state detectors with larger active areas and numbers of detector channels (Pullia *et al.*, 1996; Bucher *et al.*, 1996; Ryan *et al.*, 2010) has been enhancing the elemental sensibility suited for investigating very dilute systems with elemental concentrations in the p.p.m. and sub-p.p.m. regimes.

Most beamlines at leading synchrotron facilities around the world dedicated to XAS techniques can be classified into two groups: soft X-ray beamlines covering photon energies from 0.1 to 2 keV and hard X-ray beamlines covering photon energies above 4 keV. The energy gap between the soft and hard X-ray regions arises from diffracting elements that are practical and often chosen for dispersing the synchrotron beam, *i.e.* plane grating for soft X-rays and crystals for hard X-rays. It is noteworthy that there are, however, a few beamlines working in the intermediate photon-energy range. Table 1 provides a list of some of the beamlines in this group. One of them is beamline BL8 of the Synchrotron Light Research Institute (SLRI), Thailand. To the best of our knowledge there is little available detailed information regarding the instrumentation, performance and application of such beamlines despite their capabilities to study *K*-edges of 2*p* elements (*Z* = 11 to 17; sodium to chlorine), which are inaccessible by the hard X-ray beamlines.

In this report we will describe the technical specification of BL8 and its XAS station that has not been updated in the literature after the commissioning of TM-mode XAS (Klysubun *et al.*, 2006, 2007). During the last four years major

**Table 1**
Specification of X-ray beamlines that can provide photon energies from 2.1 keV and above.

The first 11 beamlines are compiled from a survey of 125 XAS beamlines at leading synchrotron facilities: APS, NSLS, SSRL, ESRF, SOLEIL, SPring-8, KEK, PAL and NSRRC. Our beamline is included in the last row for comparison.

| Beamline | Facility | Energy range (keV) | Beam size (mm) | Flux (photons s$^{-1}$) | Resolution |
|---|---|---|---|---|---|
| 9-BM-B | APS | 2.1–23 | 0.5 × 0.5 | 1 × 10$^{11}$ [a] | 1 × 10$^{-4}$ |
| 9-BM-C | APS | 2.1–23 | 1 × 1 | 1 × 10$^{11}$ [a] | 1 × 10$^{-4}$ |
| X15B | NSLS | 1.2–8 | <1 × 1 | 1 × 10$^{12}$ [b] | 2 × 10$^{-4}$ [c] |
| X19A | NSLS | 2.1–17 | 2 × 1 | 5 × 10$^{10}$ [d] | 2 × 10$^{-4}$ |
| ID12 | ESRF | 2.05–15 | 1 × 1 [e] | 1 × 10$^{11}$ | 1 × 10$^{-4}$ |
| ID21 | ESRF | 2.1–9.2 | 2 × 2 [e] | 7 × 10$^{10}$ | 1 × 10$^{-4}$ |
| ID32 | ESRF | 2.0–25 | 1.5 × 0.8 [e] | 10$^{12}$–10$^{13}$ | 1 × 10$^{-4}$ |
| Lucia | SOLEIL | 0.8–8 | 0.00025 × 0.00025 | 8 × 10$^{10}$ [b] | 4 × 10$^{-4}$ [g] |
| BL-2A | KEK | 1.8–5 | 1 × 1 | 2 × 10$^{11}$ [e] | 1.3–5 × 10$^{-4}$ |
| BL-9A | KEK | 2.1–15 | 1 × 0.35 | 4 × 10$^{11}$ [f] | 2 × 10$^{-4}$ [f] |
| BL16A1 | NSRRC | 2–8 | 0.5 × 0.4 | 4.8 × 10$^{11}$ [h] | 1.5–2.1 × 10$^{-4}$ |
| BL8 | SLRI | 1.2–10 | 14 × 1 | 1.3 × 10$^{9}$–6 × 10$^{10}$ | 1.3–5.4 × 10$^{-4}$ |

[a] At 15 keV. [b] At 4 keV. [c] For Si(111). [d] At 2.5 keV. [e] Maximum value. [f] At 9 keV. [g] At 2 keV. [h] At 5 keV.

developments have been focused on expanding the photon energy range, implementation of the FY-mode XAS technique in addition to the TM-mode technique, and standardization for improving data quality and throughput of the beamline. The performance of BL8 and its XAS station will be examined, in comparison with those of other XAS beamlines, in terms of spectral resolution, photon flux and limitation. Finally, applications of the XAS technique at BL8 will be discussed in general and on selected topics in the fields of material science, environmental science and cultural heritage.

## 2. Beamline

Operation of BL8 was started in late-2006 with a special design to exploit synchrotron radiation from the Siam Photon Source (1.2 GeV), a second-generation synchrotron light source, of SLRI. This beamline accepts 1.5 mrad (H) × 0.125 mrad (V) of synchrotron white light generated from a bending magnet (1.44 T) with a maximum electron beam current of 150 mA and critical energy of 1.38 keV. Based on a calculation using *SPECTRA* (Tanaka & Kitamura, 2001), the partial photon flux for this angular acceptance peaks at 5.3 × 10$^{11}$ photons s$^{-1}$ (0.1% bandwidth)$^{-1}$ (100 mA)$^{-1}$ at 1.18 keV

and drops by almost two orders of magnitude from 0.4 keV to 10 keV. A schematic representation of BL8 is shown in Fig. 1. To isolate ultra-high-vacuum (UHV; 10$^{-10}$ torr) conditions in the front-end section and high-vacuum (HV; 10$^{-6}$ torr) conditions in the downstream sections of the beamline, two differential pumping stages, each of which encompasses a small rectangular duct of low vacuum conductance (LVC) and an ion pump (IP) with high pumping speed, were employed, rather than using an ordinary beryllium window, which significantly attenuates synchrotron radiation in the soft X-ray regime. Functional testing of this differential pumping system was reported by Klysubun *et al.* (2007). It should be noted that, to date, there has never been a failure originating from this vacuum sectioning scheme. Other basic components as indicated in Fig. 1 were installed for complete function of the beamline.

To disperse synchrotron light we have employed a fixed-exit double-crystal monochromator (DCM) with a water-cooled holder for the first crystal and a holder without cooling for the second crystal. The fixed-exit condition was achieved by a Lemonnier design (Lemonnier *et al.*, 1978) in which the second crystal travels on a mechanical cam to maintain a constant offset (3 cm). The two crystals are rectangular in shape and have the same required size of 20 mm (width) × 40 mm (length) × 2 mm (thickness). Since the rotation mechanism of the DCM allows Bragg angle scanning from 13.5 to 65° at a resolution of 0.0001°, using Si(111) alone would provide a monochromatic beam only from 2.18 to 8.47 keV. Thus other types of crystal pairs, *i.e.* KTP(011), InSb(111) and Ge(220), are complementarily employed to cover a broader spectral range and are manually interchangeable. The values of the 2*d* lattice spacing of these crystals have been given elsewhere (Thompson & Vaughan, 2001; Takata *et al.*, 2001). With this set of crystals BL8 can deliver a monochromatic X-ray beam with photon energies ranging from 1.25 keV to
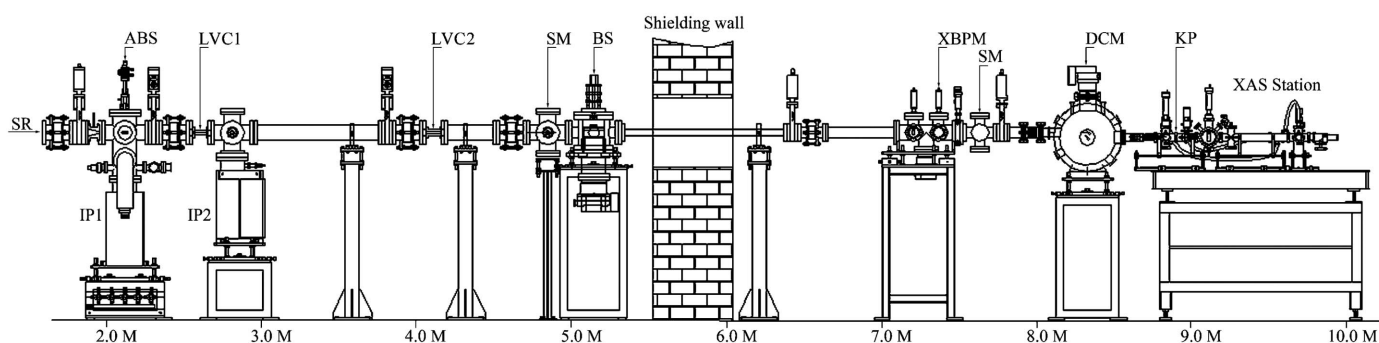


**Figure 1**
Schematic view of BL8 indicating functional components such as the heat absorber (ABS), differential pumping stages (LVC1/IP1 and LVC2/IP2), screen monitors (SM), beam shutter (BS), X-ray beam-position monitor (XBPM), double-crystal monochromator (DCM) and Kapton window (KP).

**Table 2**
Energy resolution ($\Delta E/E$) of the 1st-order radiation and higher-order radiation ratio.

| | InSb(111) | | | Si(111) | | Ge(220) | |
|---|---|---|---|---|---|---|---|
| $E$ (keV) | 2.0 | 2.5 | 3.0 | 3.0 | 5.0 | 5.0 | 7.0 |
| $\Delta E/E$ | $4.2 \times 10^{-4}$ | $4.3 \times 10^{-4}$ | $4.4 \times 10^{-4}$ | $2.0 \times 10^{-4}$ | $3.2 \times 10^{-4}$ | $2.2 \times 10^{-4}$ | $2.9 \times 10^{-4}$ |
| 2nd/1st | $9.7 \times 10^{-5}$ | $3.3 \times 10^{-4}$ | $1.2 \times 10^{-3}$ | $3.4 \times 10^{-5}$ | $6.5 \times 10^{-4}$ | $3.3 \times 10^{-3}$ | $3.9 \times 10^{-3}$ |
| 3rd/1st | $5.9 \times 10^{-4}$ | $1.7 \times 10^{-4}$ | $5.5 \times 10^{-5}$ | $2.2 \times 10^{-5}$ | $1.6 \times 10^{-5}$ | $3.7 \times 10^{-5}$ | $3.4 \times 10^{-5}$ |
| 4th/1st | $9.8 \times 10^{-5}$ | $1.8 \times 10^{-5}$ | $2.5 \times 10^{-6}$ | $2.8 \times 10^{-6}$ | 0 | 0 | 0 |

10 keV covering the $K$-edges of Mg up to Zn as well as $L_{1,2,3}$- and several $M$-edges of other heavier elements. A bypass pumping system was installed for minimizing the time used to change the crystals. Without turning off the turbomolecular pump of the DCM we can break the vacuum, replace the double crystals and re-pump the DCM to obtain HV within 30 min. There is an entrance vertical slit in the DCM chamber for optimizing the energy spread and intensity of the exit beam. It is regularly set at 1 mm corresponding to the beam divergence of 125 µrad which is about one to three times bigger than intrinsic bandwidths of most crystals in use. The energy resolution for a 125 µrad slit size is estimated theoretically as reported in Table 2. Measurement of the energy resolution is currently underway. The slit size can be further reduced to improve the energy resolution (decrease the energy spread) of the exit beam. The contribution of higher harmonics was determined using a silicon drift detector measuring the beam exiting the DCM. The obtained result is also given in Table 2. Operation of the beamline is entirely controlled by *LabVIEW* software developed in-house.

## 3. Experimental station

The experimental set-up for collecting XAS spectra in both TM and FY modes is shown in Fig. 2. From the DCM HV chamber the monochromatic beam propagates to the experimental station through a Kapton (KP) window. The window has a 14 mm circular aperture on a stainless steel centring ring (DN40 KF) and is vacuum-sealed with a KP film (7.5 µm thick). This assembly allows the window to withstand force



**Figure 2**
Experimental set-up for XAS in TM and FY modes.

exerted between HV and atmosphere. The intensities of the incident beam ($I_0$) and the transmitted one ($I_t$) are measured by the first ion chamber (IC1; 10 cm long) and the second ion chamber (IC2; 40 cm long), respectively. The beam size at the sample chamber is 14 mm (width) $\times$ 1 mm (height).

To realise the experimental set-up that can be used for XAS measurements from 1.25 to 10 keV, without any time-consuming swapping of instruments, requires careful consideration to overcome the low transmission in the low photon energy region when using the ion chambers. For an experiment performed below 4 keV, $N_2$ gas is then used to partially fill IC1 and IC2 at specific pressures absorbing 10% and 90% of the beam intensity, respectively. For instance, 4.5 torr for IC1 and 17.5 torr for IC2 are used at the $K$-edge of Mg (1303 eV). Note that air can also be used, but should be avoided around 3.2–3.3 keV owing to the $K$-edge absorption of Ar itself. On the other hand, Ar gas is used for experiments at higher photon energies. For instance, 70 torr for IC1 and 382 torr for IC2 are employed at the $K$-edge of Zn (9659 eV). To facilitate gas filling below atmospheric pressure, the ion chambers are made of KF-flange vacuum-tight vessels. The first ion chamber is fit to the KP window and thereby sealed with it at the front. Polypropylene (PP) windows (6 µm thick) fabricated similarly to the KP window were used to separate IC1 and IC2 from the sample chamber and to seal the gas within them. Note that PP is chosen over KP owing to its higher transmittance which is more than a factor of two for photon energies below 1.5 keV. However, the PP windows are less resistant than the KP window and often break when evacuating the ion chambers for changing gas conditions. For this reason the ion chambers are needed to be filled up with He gas to atmospheric pressure to reduce the risk of window damage during the experiment. A dosing valve (DV), angle valves (AV) and capacitance gauges (CG), as shown in Fig. 2, enable precise adjustment of the gas condition for a given edge of the element being studied.

A 13-element germanium detector (Canberra Ultra-LEGe; GeD), a single-element silicon drift detector (Vortex-EM; SDD) and a five-grid ion chamber (Lytle detector; LyD) are available choices for an FY-mode XAS experiment. With signal averaged over the 13 channels, the energy resolution of the GeD at 5.9 keV (with 8 µs peaking time) was 169 eV while that of SDD (with 1 µs peaking time) was 189 eV. As shown in Fig. 2, the GeD is placed at 90° to the incident beam and 45° to the irradiated sample surface. The SDD or LyD is oriented in the same manner on the opposite side. For an experiment below 4 keV the sample chamber is purged with He gas to minimize absorption by air, as is the case in TM-mode. A gas-
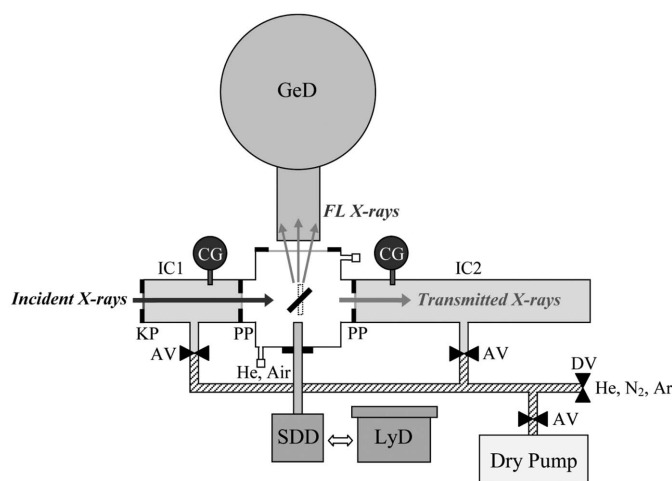
tight PP window centred on a centring ring (DN100 ISO) facing the GeD elements prevents He gas from penetrating the detector Be window (25.4 µm) and deteriorating the HV in the GeD. Thus, the closest sample-to-detector distance allowed for the GeD is 6 cm. For the SDD, it has smaller active area (50 mm$^2$) than that of the GeD (1300 mm$^2$), and therefore it has to be placed closer to the sample inside the sample chamber. This increases the solid angle for accepting fluorescence signals; as a result its sensitivity is almost comparable with that of the GeD for studying elements in the low concentration limit. On the other hand, the LyD has been proven most practical in the case that elemental concentration is too low to obtain a sufficient edge jump in a TM-mode XAS spectrum, but still too high that the fluorescence signal causes high dead-time (>30%) for the GeD. An *in situ* cell is available for TM-XAS experiments under controllable heating temperature (298–673 K) and reaction gases (Loiha *et al.*, 2011).

Four modules of digital X-ray processor (XIA DXP-XMAP) on a National Instruments (PXI-1042) crate were employed for counting X-ray photons from 13 channels of the GeD and one of the SDD. The shaping time for the multichannel analyser can be defined according to the input rate of the X-ray signal. This can be conveniently parameterized using *X-Manager* software supporting the XIA processor. It should be noted that typical X-ray fluorescence spectra of a given sample can also be collected in addition to XAS spectra. A region of interest and integration time can also be defined for the processor to count fluorescent photons, commonly enclosing the $K_\alpha$ line, of an absorbing element in the sample. All selected parameters are then saved in a configuration file for execution during XAS data acquisition. Detector deadtime was simply corrected using the ratio of input rate and output rate from the processor (Woicik *et al.*, 2010). Current amplifiers are used to magnify electrical currents from the ion chambers, typically in the range 1–100 nA. The voltage outputs from the current amplifiers are fed into a V/F converter to generate a pulsed signal at the rate of 0.1 MHz V$^{-1}$. A counter/timer imposes gating on this pulsed signal input to synchronize its counting with the XIA processor. *LabVIEW* data acquisition software is developed in-house to control all of the electronics and DCM scanning during XAS data collection.

## 4. Performance and status of BL8 for XAS

During the first two years of operation BL8 covered photon energies from 1.8 keV to 9 keV by using three types of crystals: InSb(111), Si(111) and Ge(220). To disperse softer X-rays a pair of KTP(011) was procured afterwards. In addition, the increase of electron beam energy (from 1.0 GeV to 1.2 GeV) and the electron beam current (from 100 mA to 150 mA) of our storage ring has made available sufficient photon flux for XAS experiments up to 10 keV. Measured by the ion chamber IC1, the photon fluxes at the sample obtained with different crystals are shown in Fig. 3. The present KPT(011) used in our DCM yields photon flux from $1 \times 10^9$ to $4 \times 10^9$ photons s$^{-1}$
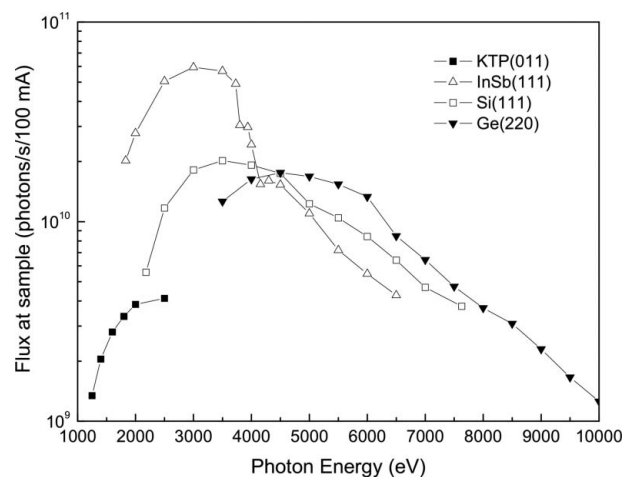


**Figure 3**
Photon flux at the sample for a beam size of 14 mm (H) × 1 mm (V), obtained from several DCM crystals used at BL8.

$(100 \text{ mA})^{-1}$ in the 1.25–2.5 keV range. Takata *et al.* (2001) underlined that KTP(011) performed better than YB$_{66}$ by giving a ten times higher flux with comparable resolving power. Moreover, we found that YB$_{66}$ was difficult to obtain and thereby of very high price. KTP(011) is thus our choice for measuring the *K*-edges of Mg and Al. Examples of Mg *K*-edge XANES spectra taken with KTP(011) will be displayed in the following section.

It should be noted that the highest flux is obtained with InSb(111) in the 1.8–3.5 keV range, making our XAS station exceptional for studying Si, P, S and Cl at the low concentration limit (∼50 p.p.m.). Nonetheless, there is an intensity drop-off between 3.6 keV and 4.7 keV owing to the *L*-edges absorption of In and Sb themselves. Ge(220) is often used for elements with absorption edges above 3.5 keV because its throughput is higher than that of Si(111) owing to its larger energy width (<12% difference). As a consequence the intrinsic energy resolution of Ge(220) is slightly poorer than that of Si(111). The overall flux at our XAS station in the 4–10 keV range is about $10^{10}$–$10^9$ photons s$^{-1}$ $(100 \text{ mA})^{-1}$.

For evaluation of spectral quality, Cu *K*-edge copper-foil XANES spectra taken at BL8 using Ge(220) crystals and similar data from other beamlines using Si(111) and Si(311) crystals are compared in Fig. 4. In general, all spectra exhibit consistently the XANES fingerprint of metallic (f.c.c.) copper. The first peak at 8981 eV, which corresponds to the 1*s*–4*p* transition (Kim *et al.*, 2003), shown in the BL8 spectra is broader than those in the X23A, ID10 and ID13 spectra. Nonetheless, it became more pronounced when the size of the DCM entrance slit was decreased from 1 mm to 0.5 mm as shown by the green and red curves, respectively. We cite a compilation of a larger number of copper-foil spectra by Kelly *et al.* (2009). Carefully examining those spectra we found that peak broadening similar to our case is also observed in the spectra from BL01 (SPring-8) and BL2-3 bulk (SSRL) although they were scanned with Si(111) monochromators. We have also evaluated the stability of the DCM, by successively scanning EXAFS spectra of the copper foil and examining the
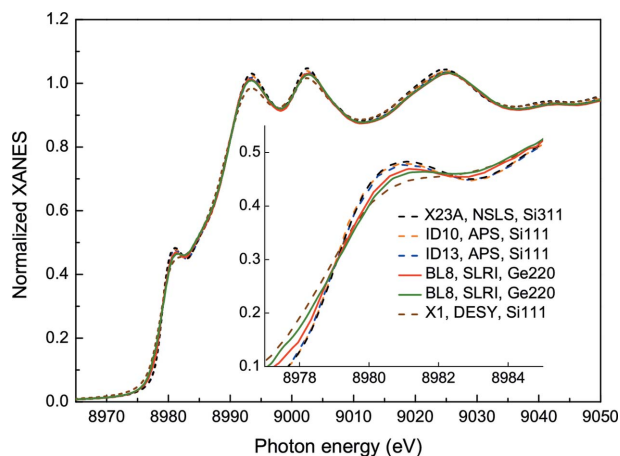
**Figure 4**
Cu $K$-edge XANES spectra of copper foils from different beamlines.

shift in the edge position, which is commonly caused by heat load on the DCM crystals and electron beam instability. For 46 spectra measured in 8 h 15 min, using the same energy range (8949–9839 eV), interval (0.3 eV and 0.05 Å$^{-1}$) and dwell time (1 s) for all scans, the resulting shift was $0.07 \pm 0.09$ eV.

The quality of the EXAFS data acquired by the XAS station at BL8 is demonstrated in Fig. 5. It shows that our EXAFS technique in the TM-mode has been standardized as seen by the good agreement in the oscillatory pattern of the copper-foil EXAFS signal compared with those obtained from the aforementioned beamlines. Fourier-transformed in the $k$ range between 3 and 13 Å$^{-1}$, the magnitude of the first peak in the BL8 data plotted in real space ($R$) shows only a 1.6% difference from that of the X23A data, which corresponds to an the ideal amplitude reduction factor ($S_0^2$) of 1 (Kelly *et al.*, 2009). Determined from the difference between the raw data and the polynomial spline in the high-$k$ region (16–22 Å$^{-1}$; 9956–10826 eV) of the Cu-foil data, a low residue noise of $2.1 \times 10^{-4}$ was obtained. At other energy ranges we found that
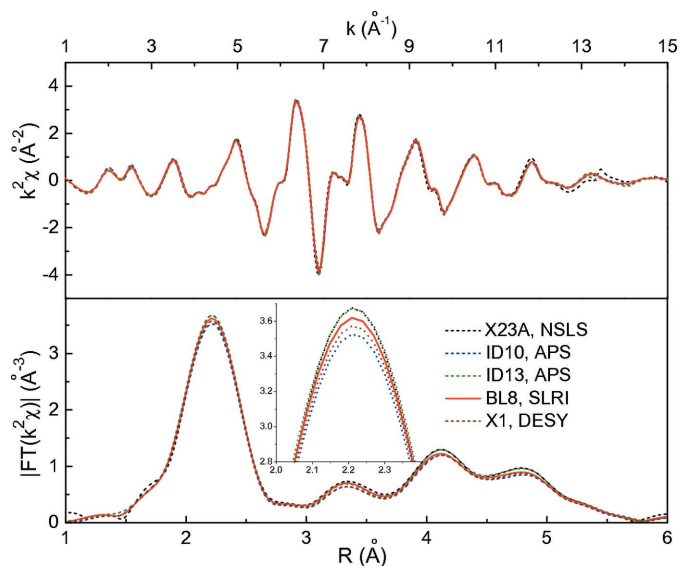
the EXAFS residue noise was $3.3 \times 10^{-4}$ and $2.0 \times 10^{-3}$ above the Ti $K$-edge (5943–6813 eV) and P $K$-edge (3120–3993 eV), respectively. The large residue at the 3 keV range probably arises from beam contamination of higher harmonics and the $L$-edge absorption of InSb(111) crystals.

In FY-mode, a similar spectral comparison could be useful for the same evaluative purpose provided there was a standard material with a specific low concentration of an absorbing element to be measured at different beamlines. In the absence of such information we can only mention that the photon flux for the FY-XAS technique is moderate compared with the photon flux of the beamlines listed in Table 1. However, the signal-to-noise ratio can be improved by increasing the integration time of the FY detection. In the following section some FY-XAS spectra of diluted samples will be presented as examples of several successful XAS experiments carried out at BL8 on diluted systems resulting in 20 publications in the year 2011.

Realising that many research works using XAS characterizations, in particular elemental speciation, require reference materials, we provide, for international XAS communities, open access to numerical data of XANES and EXAFS spectra of numerous standard compounds containing Mg, Al, Si, P, S, Cl, P, Ca and 3$d$ transition elements. The reader is invited to obtain the data at the website of BL8 (http://www.slri.or.th/).

## 5. Examples of research carried out at BL8

The number of proposals applying for beam time at BL8 has been steeply increasing from four proposals in 2006 to 100 proposals in 2011. A variety of accepted proposals during the last two years comprise studies of novel ceramics (26%), catalysts (27%) and polymers (9%), environmental (16%), geological and archaeological samples (10%) and others. In this section we illustrate three research outputs that are the result of the special character of BL8 and its station. The first example highlights the advantages of BL8's ability to perform measurements in the intermediate photon energy range. The second example highlights the advantages of strong photon flux around the S $K$-edge. The final example illustrates how a domestic synchrotron XAS station benefits archaeological research in Thailand.

### 5.1. Structural determination of MgO–ZnO alloys

Limpijumnong *et al.* (2011) measured a set of Mg and Zn $K$-edge XANES spectra from a series of Mg$_x$Zn$_{1-x}$O nanocrystals ($x = 0$–1) measured at the $K$-edges of Mg and Zn. The nanocrystal samples were synthesized by oxalate-based coprecipitation methods. Traditional X-ray diffraction (XRD) measurements could identify the overall crystal phase of the samples. It was found that the dominant phases were wurtzite (WZ) structure (common phase of ZnO) for the samples with $x \leq 0.06$ and the rocksalt (RS) structure (common phase of MgO) for $x \geq 0.09$. However, the XRD analysis could not provide information regarding the miscibility of Mg in ZnO and Zn in MgO as well as site occupations of Mg and Zn in the
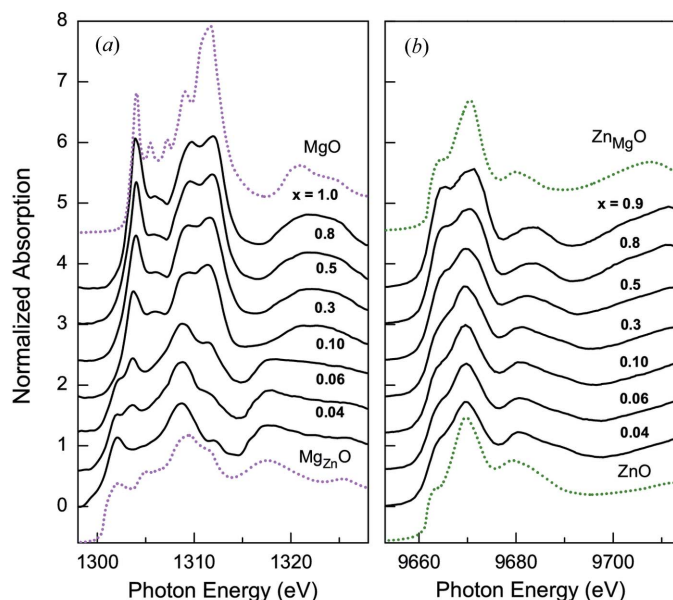


**Figure 5**
Cu $K$-edge EXAFS spectra of copper foils from different beamlines.

**Figure 6**
K-edge XANES spectra of (a) Mg and (b) Zn in $Mg_xZn_{1-x}O$ nanocrystals where x labels the Mg molar fraction. The solid and dotted lines indicate measured and calculated spectra, respectively. Spectra are vertically shifted for clarity.



**Figure 7**
Result of a linear combination fit (LCF) for a K-edge XANES spectrum of sulfur in a soil sample (Stagnosol He horizon). The solid and dotted lines represent measured spectra of relevant standards summed up to the best-fitted curve and the residual of the LCF, respectively.

samples. On the other hand the XANES spectra, as shown in Fig. 6, importantly contain the local structure information around the cations. With supporting *FEFF* calculations it was proved that the alloy samples contain four mixed phases: (i) MgO, (ii) Mg substituting Zn in WZ (tetrahedral oxide), (iii) ZnO and (iv) Zn substituting Mg (octrahedral oxide). The phase fractions were effectively determined by a least-squares linear combination fitting (LCF) method. This confirms that accurate XANES data from our beamline reveal significantly more structural information than can be obtained by traditional XRD.

### 5.2. Sulfur speciation in soils

Sulfur is naturally abundant and plays a crucial role in the environment, such as retention and remobilization of S in soils and wetlands regulating soil and water acidification and toxicity. Understanding the chemical variation of S in soils is a basic knowledge in many aspects ranging from biogeochemical S cycling in oxic and anoxic conditions to prediction of long-term S budgets of forest ecosystems. However, it is quite complicated because S exists in a large variety of organic and inorganic forms with various oxidation states, ranging from −2 (inorganic sulfide) to +6 (sulfate), and soil scientists therefore have to rely on accurate quantification of distinct sulfur species. Prietzel *et al.* (2011) demonstrated that K-edge XANES fingerprinting is more sensitive to the oxidation state of sulfur than traditional wet-chemical fractionation (WCT). For different horizons of soils, they obtained the compositional ratio of FeS, pyrite, sulfate, organic disulfide, thiol, sulfoxide, sulfone and sulfonate using the results of LCF on their measured XANES spectra. It is the incapability of WCT to distinguish the last five species of carbon-bonded S that singled out XANES as a more powerful analytical method.
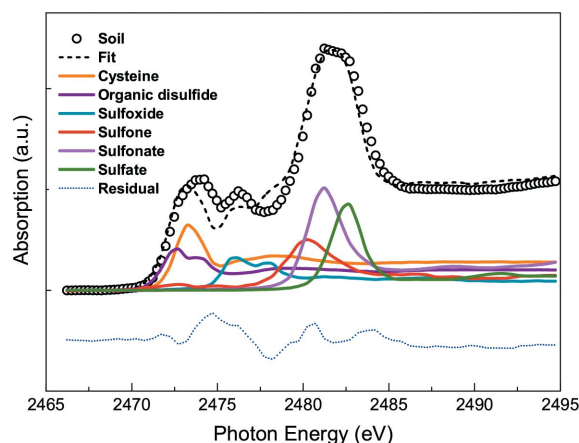
Fig. 7 shows the LCF result on Stagnosol He horizon soil, with a total S concentration of 4 g kg$^{-1}$, measurable using the GeD of BL8. Moreover, the large beam size of BL8 facilitates bulk analysis on heterogeneous samples, as is the case in soil research.

### 5.3. Oxidation states of copper in ancient red beads

Utilization of synchrotron light at BL8 in the field of archaeology was recently described by Klysubun *et al.* (2011) in their XAS study of copper as a key element in the red colouration of ancient glass beads (1300–2000 years old) excavated from four different southern archaeological sites of Thailand. The concentration of copper in the samples varied from 0.8 to 1.6 wt%. The Cu K-edge XANES data showed a superimposition of pronounced near-edge peak of monovalent copper ions ($Cu^{+1}$) and a subtle post-edge fingerprint of metallic copper ($Cu^0$). To obtain structural parameters the authors further investigated the measured EXAFS spectra, Fourier-transformed in the 2–8 Å$^{-1}$ range, and fit them with a structural model combining the f.c.c. structure and the first shell of two oxygen neighbours. The experimental data fit nicely with the proposed model as shown in Fig. 8. From this result one cannot rule out a colouring mechanism arising from surface plasma absorption by the metallic copper, provided it is present on a nanometre scale. It is interesting to note that XANES data of red glass cakes and mosaics from Messina, Italy (Arletti *et al.*, 2008), noticeably resemble the XANES data of the red glass beads from Thailand. This suggests that ancient knowledge in making red glass may be historically common or transferred *via* long-distance trading between the two regions.

### 6. Conclusion

Specifications and instrumentation of BL8 are reported in detail, including the end-station for conducting XANES and EXAFS experiments in TM and FY modes. The available
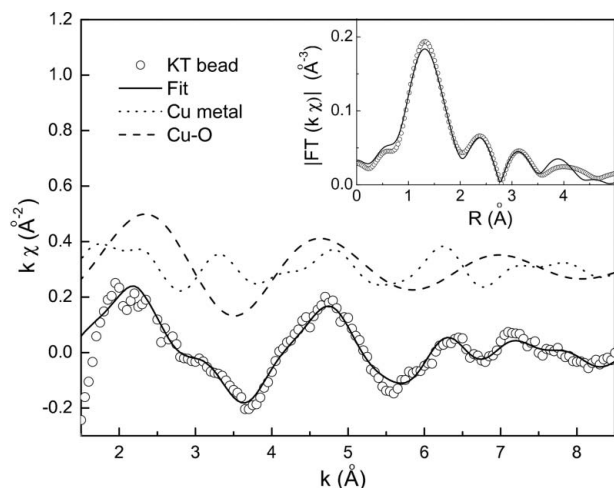
**Figure 8**
EXAFS spectrum of an ancient bead from Khlong Thom archaeological site, Thailand. Solid, dotted and dashed lines represent the best-fitted curve, deconvoluted Cu metallic and Cu—O components, respectively. The insert shows the magnitudes of Fourier-transformed spectra of the sample and the best-fitted curve.

photon energy scanned by the DCM, which is equipped with KTP(011), InSb(111), Si(111) and Ge(220), ranges from 1.25 to 10 keV. The resulting photon flux was measured to be $10^9$–$10^{10}$ photons s$^{-1}$ (100 mA)$^{-1}$ with an energy resolution of 1.3–$5.4 \times 10^{-4}$, depending on the type of crystals used. The beam size at the sample position is 14 mm × 1 mm. Standard pulse-counting electronics were employed for processing the XAS signals in both TM and FY modes.

In TM mode the performance of BL8 was characterized using a standard copper foil. The measured Cu $K$-edge spectra exhibit XANES and EXAFS structures consistent with the spectra obtained from other well established beamlines: X23A (NSLS), ID10 and ID13 (APS) and X1 (DESY). It was demonstrated that the spectral resolution could be influenced by the size of the vertical entrance slit of the DCM and the bandwidth of the DCM crystals.

In FY mode the 13-element Ge detector makes it possible to obtain good quality spectra for low-concentration absorbing elements irradiated by the moderate photon flux at BL8. This is confirmed by publishable spectra of Mg and Zn $K$-edge XANES of MgO–ZnO alloys, S $K$-edge XANES of soils and Cu $K$-edge XANES and EXAFS of ancient red beads, among other outputs of the beamline in 2011.

As a final remark BL8 is one of the intermediate energy beamlines around the world that exist in a much smaller number than the hard X-rays beamlines and the soft X-rays beamlines. Aside from the standardized performance, the attractiveness of BL8 stems from the convenience of changing experimental conditions from one absorption edge to another and provision of a large beam size well suited to bulk analysis, especially for heterogeneous and composite samples in the fields of environmental and archaeological sciences.

## References

Arletti, R., Quartieri, S., Vezzalini, G., Sabatino, G., Triscari, M. & Mastelloni, M. A. (2008). *J. Non.-Cryst. Solids*, **354**, 4962–4969.

Baldini, M., Yang, W., Aguilanti, G., Zhang, L., Ding, Y., Pascarelli, S. & Mao, W. L. (2011). *Phys. Rev. B*, **84**, 014111.

Bucher, J. J., Allen, P. G., Edelstein, Shuh, D. K., Madden, N. W., Cork, C., Luke, P., Pehl, D. & Malone, D. (1996). *Rev. Sci. Instrum.* **67**, 3361.

Cotte, M., Susini, J., Dik, J. & Janssens, K. (2010). *Acc. Chem. Res.* **43**, 705–714.

Day, A., Broderick, W. E., Hedman, B., Hodgson, K., Broderick, J. B. & Solomon, E. I. (2011). *J. Am. Chem. Soc.* **133**, 18656–18662.

Freedman, L. P., Luisi, B. F., Korszun, Z. R., Basavappa, R., Sigler, P. B. & Yamamoto, K. R. (1988). *Nature (London)*, **334**, 543–546.

Kelly, S. D., Bare, S. R., Greenlay, N., Azevedo, G., Balasubramanian, M., Barton, D., Chattopadhyay, S., Fakar, S., Johannessen, B., Newville, M., Pena, J., Pokravski, G. S., Proux, O., Priolkar, K., Ravel, B. & Webb, M. (2009). *J. Phys.* **190**, 102032.

Kim, W. B., Park, E. D., Lee, C. W. & Lee, J. S. (2003). *J. Catal.* **218**, 334–347.

Klysubun, W., Sombunchoo, P., Wongprachanukul, N., Tarawarakarn, P., Klinkhieo, S., Chaiprapa, J. & Songsiriritthigul, P. (2007). *Nucl. Instrum. Methods Phys. Res. A*, **582**, 87–89.

Klysubun, W., Tarawarakarn, P., Sombunchoo, P., Klinkhieo, S., Chaiprapa, J. & Songsiriritthigul, P. (2006). *AIP Conf. Proc.* **879**, 860–863.

Klysubun, W., Thongkam, Y., Pongkrapan, S., Won-in, K., T-thienprasert, J. & Dararutana, P. (2011). *Anal. Bioanal. Chem.* **399**, 3033–3040.

Lemonnier, M., Collet, O., Depautex, C., Esteva, J. & Raoux, D. (1978). *Nucl. Instrum. Methods*, **152**, 109–111.

Limpijumnong, S., Jutimoosik, J., Palakawong, N., Klysubun, W., Nukeaw, J., Du, M.-H. & Rujirawat, S. (2011). *Appl. Phys. Lett.* **99**, 261901.

Loiha, S., Klysubun, W., Khemthong, P., Prayoon pokarach, S. & Wittayakun, J. (2011). *J. Taiwan Inst. Chem. E*, **42**, 527–532.

Neidig, M. L., Sharma, J., Yeh, H. C., Martinez, J. S., Conradson, S. D. & Shreve, A. P. (2011). *J. Am. Chem. Soc.* **133**, 11837–11839.

O'Day, P. A., Carroll, S. A. & Waychunas, G. A. (1998). *Environ. Sci. Technol.* **32**, 943–955.

Prietzel, J., Botzaki, A., Tyufekchieva, N., Brettholle, M., Thieme, J. & Klysubun, W. (2011). *Environ. Sci. Technol.* **45**, 2878–2886.

Pullia, A., Furenlid, L., Kraner, H. W., Pietrski, P. J. & Siddons, D. P. (1996). *Rev. Sci. Instrum.* **67**, 3360.

Radisavljevic, I., Novakovic, N., Romcevic, N., Manasijecvic, M., Mahnke, H.-E. & Ivanovic, N. (2010). *J. Alloys Compd.* **501**, 159–163.

Ryan, C. G., Kirkham, R., Hough, R. M., Moorhead, G., Siddons, D. P., de Jonge, M. D., Paterson, D. J., De Geronimo, G., Howard, D. L. & Cleverley, J. S. (2010). *Nucl. Instrum. Methods Phys. Res. A*, **619**, 37–43.

Suksabye, P., Thiravetyan, P., Nakbanpote, W. & Chayabutra, S. (2007). *J. Hazard. Mater.* **141**, 637–644.

Takata, Y., Shigemasa, E. & Kosugi, N. (2001). *J. Synchrotron Rad.* **8**, 351–353.

Tanaka, T. & Kitamura, H. (2001). *J. Synchrotron Rad.* **8**, 1221–1228.

Thompson, A. & Vaughan, D. (2001). *X-ray Data Booklet.* Lawrence Berkeley National Laboratory, University of California, California, USA.

Woicik, J. C., Ravel, B., Fischer, D. A. & Newburgh, W. J. (2010). *J. Synchrotron Rad.* **17**, 409–413.